Biopolymer-assisted Synthesis of P-doped TiO$_2$ Nanoparticles for High-performance Lithium-ion Batteries: A Comprehensive Study

Nabil El Halya,[a] Mohamed Aqil,[a] Karim El Ouardi,[a, b] Amreen Bano,[d] Ayoub El Bendali,[a] Loubna Hdidou,[a] Rachid Amine,[c] Seoung-Bum Son,[c] Fouad Ghamouss,[a] Dan Thomas Major,[d] Khalil Amine,[c] Jones Alami,[a] and Mouad Dahbi*[a]

TiO$_2$ material has gained significant attention for large-scale energy storage due to its abundant, low-cost, and environmentally friendly properties, as well as the availability of various nanostructures. Phosphorus doping has been established as an effective technique for improving electronic conductivity and managing the slow ionic diffusion kinetics of TiO$_2$. In this study, non-doped and phosphorus doped TiO$_2$ materials were synthesized using sodium alginate biopolymer as chelating agent. The prepared materials were evaluated as anode materials for lithium-ion batteries (LIBs). The electrodes exhibit remarkable electrochemical performance, including a high reversible ca-

pacity of 235 mAh g^{-1} at 0.1 C and excellent first coulombic efficiency of 99%. An integrated approach, combining operando XRD and ex-situ XAS, comprehensively investigates the relationship between phosphorus doping, material structure, and electrochemical performance, reinforced by analytical tools and first principles calculations. Furthermore, a full cell was designed using 2%P-doped TiO$_2$ anode and LiFePO$_4$ cathode. The output voltage was about 1.6 V with high initial specific capacity of 148 mAh g^{-1}, high rate-capability of 120 mAh g^{-1} at 1 C, and high-capacity retention of 96% after 1000 cycles at 1 C.

Highlights

- The use of sodium alginate as complexing agent during P doping of TiO$_2$ shows beneficial effect on P distribution and electronic conductivity of TiO$_2$ electrodes.
- P-doped TiO$_2$ electrodes delivers high-reversible capacity of 235 mAh g^{-1} at 0.1 C and excellent first coulombic efficiency of 99%.

- Structural evolution during cycling and electronic structure of the prepared materials were investigated using Operando XRD and XAS spectroscopy.
- The experimental results were reinforced by the application of analytical tools and first principles calculations.
- High-performance full lithium-ion battery was designed using 2%P-doped TiO$_2$ anode and LiFePO$_4$ cathode.

[a] N. El Halya, M. Aqil, K. El Ouardi, A. El Bendali, L. Hdidou, F. Ghamouss, J. Alami, M. Dahbi
Materials Science, Energy, and Nano-engineering Department
Mohammed VI Polytechnic University
Ben Guerir (Morocco)
E-mail: Mouad.Dahbi@um6p.ma

[b] K. El Ouardi
Laboratory of Physic-Chemistry, Materials and Catalysis, department of chemistry
Faculty of Sciences Ben M'sik
University Hassan II of Casablanca
Casablanca (Morocco)

[c] R. Amine, S.-B. Son, K. Amine
Chemical Sciences and engineering Division
Argonne National Laboratory
9700 S. Cass Avenue Lemont, IL 60439 (USA)

[d] A. Bano, D. T. Major
Department of Chemistry and Institute of Nanotechnology and Advanced Materials
Bar-Ilan University
Ramat-Gan 52900 (Israel)

Introduction

Lithium-ion batteries (LIBs) find extensive application in portable electronic devices, electric vehicles, and energy storage systems, thanks to their impressive energy density and extended cycling capabilities.[1–3] However, the performance of LIBs is limited by the capacity and stability of the anode materials, which play a critical role in the overall performance of the battery.[4] Conventional graphite anodes have been widely used for lithium-ion batteries thanks to their low cost, large natural abundance, good cycling stability and excellent electrical conductivity.[5–7] However, their theoretical capacity limit is reaching its maximum limit of approximately 372 mAh g^{-1}.[8,9] To overcome the limitations of graphite, researchers are continuously investigating higher capacity and superior performance anode materials. One promising approach is the use of silicon-based materials, which can store up to ten times more lithium than graphite. Nonetheless, silicon-based anodes experience significant capacity decay and limited cycling stability as a result of the huge volume changes during lithiation delithiation process.[10–13] Other materials being researched include metal oxides,[14] metal sulfides,[15] and carbon-based materials such as

Batteries & Supercaps

Research Article
doi.org/10.1002/batt.202300424

Chemistry
Europe

European Chemical
Societies Publishing

carbon nanotubes and graphene.[16] These materials have shown promising results in terms of capacity and stability, but further research is needed to optimize their performance and address the challenges.

Titanium dioxide (TiO$_2$) has emerged as a promising option for the negative electrode material in LIBs due to its impressive characteristics. Its higher lithium insertion potential and thermodynamic stability compared to graphite make it less susceptible to lithium dendrites formation, thereby enhancing safety. Additionally, TiO$_2$ exhibits minimal volume variation (less than 4%) during charge/discharge cycles and is both affordable and environmentally sustainable.[17,18] Despite these advantages, the expected rapid adoption of TiO$_2$ as a negative electrode material in LIB industry has not been achieved. The major impediment to the broader use is its poor electronic conductivity, which significantly limits its performance under high charge/discharge currents.[17] Numerous innovative strategies have been successfully deployed to address the low electronic conductivity of TiO$_2$. One notable technique involves reducing the particle size, which has shown considerable promise in enhancing the material's conductivity and overall performance. However, self-aggregation during the charge/discharge process remains a major problem which causes a huge capacity drop.[19] The advantage of nanoparticles can be preserved by employing various hierarchical nanostructures such as microspheres, porous nanostructures, etc.[20–27] which effectively prevents the aggregation of nanoparticles. However, the preparation techniques of these nanostructures generally involve specific reagents, extended reaction durations time and complex process. Another promising approach involves utilizing perfectly crystallized TiO$_2$ anatase, which exhibits superior electrochemical performance and better electrical conductivity.[28–30] Nevertheless, the production of TiO$_2$ anatase with high crystallinity generally requires high temperatures treatment, which can lead to structure degradation, particle size increase and transformation of the crystalline phase.[28,31] Alternatively, to obtain a more conductive phase, doping or modification with heteroatoms or electronically conductive materials (graphene, CNTs, etc.) seems to be good strategies.[32–35] However, these methods usually require complicated preparation. Therefore, it would be desirable to find a simple, inexpensive, and efficient preparation process to synthetize TiO$_2$ anatase nanoparticles with high electronic conductivity.

In this paper, we are interested in developing a simple and inexpensive strategy for the synthesis of phosphorus doped TiO$_2$ nanoparticles. In fact, our strategy involves the use of sodium alginate biopolymer to facilitate the incorporation of phosphorus ions into the TiO$_2$ lattice during the Sol-Gel

synthesis. Moreover, investigating the effect of phosphorus doping on the structure and electrochemical performance of TiO$_2$. To gain deeper insights, we utilized a combination of analytical tools, electrochemical tests and first principles calculations to understand the reasons behind the impact of P-doping in the battery performance. Our research revealed that 2%P doping of TiO$_2$ electrode resulted in a significant improvement in first coulombic efficiency, specific capacity, cycling stability, and rate capability compared to the non-doped electrode.
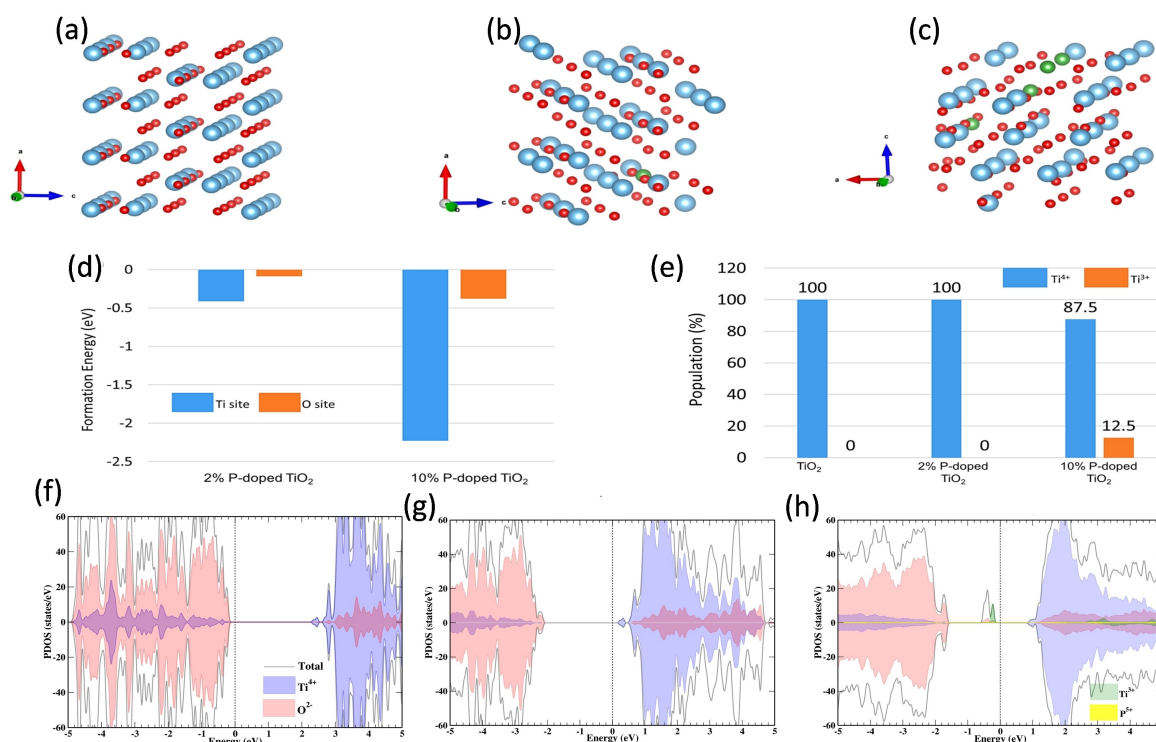
Results and Discussions

Materials characterizations

The crystal structures of the prepared materials were identified by XRD (Figure S2a) followed by Rietveld refinement (Figure S3). In addition, the crystallographic information obtained from the refinement of all samples is presented in Table 1. The diffraction peaks 25.3°, 37.9°, 48.1°, 54.7°, 55.0°, 62.7°, 68.9°, 75.04°, 83.0° are ascribed to (101), (004), (200), (105), (211), (204), (116), (215), (312) diffraction planes of anatase TiO$_2$, respectively.[36–39] Moreover, the phosphorus characteristic peaks are absent in all patterns, which could be attributed to the high phosphorus dispersion or the low doping concentration. According to Fan et al., below 873 K, phosphorus exists as amorphous titanium phosphate within the TiO$_2$ nanoparticles.[40] Furthermore, the XRD patterns do not reveal any additional diffraction peaks corresponding to impurities, suggesting the high purity of the prepared materials. Raman spectroscopy was employed to further investigate the structural characteristics of non-doped and P-doped TiO$_2$ materials (Figure S2b). The resulting bands at 198, 400, 518, and 641 cm^{-1} present the Raman-active vibrational modes of anatase TiO$_2$.[41] The peaks of the rutile and brookite phase (JCPDS card no. 21-1276 and JCPDS card no. 29-1360) are not clearly identified in the three samples. The XRD and Raman findings provide compelling evidence that the obtained TiO$_2$ nanoparticles possess an anatase crystal structure. Additionally, computationally obtained optimized geometries of pristine TiO$_2$ along with 2% P and 10% P doped TiO$_2$ are shown in Figure 1(a–c). To find suitable dopant sites for P, we employed MCSA simulations implemented in the GULP code[42–44] to generate 20,000 possible configurations. The lowest energy structure was then considered for further optimizations using DFT. The computed formation energy (Figure 1d) for dopant sites suggests that Ti-sites are preferred over O-sites. Structural parameters of the fully optimized

Table 1. X-ray diffraction Rietveld structural analysis of non-doped and P-doped TiO$_2$ powders.

Sample structure	Phase		$a=b$ [Å]		c [Å]		Space group	Volume [Å]		$\alpha=\beta=\gamma$
			Exp	DFT	Exp	DFT		Exp	DFT	
Non-doped	Tetragonal	Anatase	3.79	3.79	9.49	9.51	I 41/a m d	136.43	137.92	90°
2%P-doped	Tetragonal	Anatase	3.79	3.79	9.49	9.51	I 41/a m d	136.43	137.99	90°
10%P-doped	Tetragonal	Anatase	3.80	3.81	9.50	9.52	I 41/a m d	137.41	139.08	90°

Batteries & Supercaps

Research Article
doi.org/10.1002/batt.202300424

Chemistry Europe
European Chemical
Societies Publishing

Figure 1. Computationally optimized geometries of a) non- doped, b) 2%P-doped and c) 10%P-doped TiO_2 materials. d, e) Computed formation energy for dopant sites, and Electronic Density of State of f) non-doped, g) 2%P-doped and h) 10%P-doped TiO_2 materials.

pristine and doped-TiO_2 are listed in Table 1. The lattice parameters derived from computational methods align with experimental findings.

The plots generated by the Rietveld refinement of all materials are depicted in Figure S3. The observed and calculated diffractograms are in good agreement. Besides, it is important to notice that phosphorus concentration increases the lattice parameters "*a*" and "*c*," as well as the volume, indicating that phosphorus was not only deposited on the surface, but also went into the TiO_2 crystal lattice. The increase in lattice parameters may be attributed to reduction of $Ti^{4+} \rightarrow Ti^{3+}$ at 10% P-doping, as the ionic radii of Ti^{4+} (0.605 Å) is lower than Ti^{3+} (0.67 Å). In Figure 1(e) it can be seen that at a low-level doping, i.e., 2%-doped TiO_2, no such Ti^{4+} reduction occurs. However, at higher level of doping, i.e., 10% P-doping, we estimate that 12.5% Ti^{4+} ions are reduced to Ti^{3+} ions based on magnetic moments from our DFT calculations. Therefore, a slight increase in structural parameters for the 10% P-doped material is expected.

Scanning Electron Microscopy (SEM) images of TiO_2 and P-doped TiO_2 materials are shown in Figure S4(a–c). The non-doped material shows a morphology with uniform sizes and a relatively homogeneous granular surface. After phosphorus doping, the morphology and size of the P-doped TiO_2 samples were nearly unaffected. The energy dispersive X-ray (EDX) spectroscopic data of the prepared materials (Figure S4d–f) demonstrates a homogeneous distribution of O, Ti, and P without the presence of any additional impurity elements.

The specific surface area was calculated using the Brunauer-Emmett Teller (BET) method, using nitrogen adsorption and desorption isotherms measured at a temperature of 77 K. Figure S5 displays the isotherms for nitrogen adsorption and desorption for both TiO_2 and P-doped TiO_2, along with the corresponding pore size distribution curves. The following table summarizes the results of the BET surface and the average pore width for the prepared materials.

All the materials exhibited characteristic IV adsorption/desorption isotherms indicative of mesoporous structures. Moreover, they displayed highly comparable BET surface areas, pore size distributions, and mesopore diameters. As a result, the textural attributes of the investigated materials are notably analogous. Textural parameters are summarized in Table 2.

Figure S6(a) illustrates the FT-IR spectra of the prepared materials. The broad peaks at 3404 cm^{-1} and 1632 cm^{-1} could be indexed to stretching and bending of the OH hydroxyl groups in H_2O, respectively.[45–47] Furthermore, the spectral bands within the range of 400–700 cm^{-1} can be attributed to

Table 2. The BET surface and the average pore width of the synthesized materials.

| %P	BET area [m²/g]	The average pore width [Å]	
		Adsorption	Desorption
Non-doped	80	47	43
2%P-doped	82	40	37
10%P-doped	80	30	31

the vibration modes associated with the stretching of Ti–O–Ti within the TiO_2 structure.[45,48] When compared to pure anatase, the doped materials show a modest extra absorption peak at roughly 1050 cm^{-1}. Bhaumik and Inagaki suggested that this peak could result from Ti–O–P vibrations.[48] The absence of any peaks falling within the 600 to 800 cm^{-1} range indicates that the vibration associated with P–O–P (occurring at approximately 750 cm^{-1}) is not present in the doped samples. This suggests that phosphorus is incorporated into the TiO_2 structure by creating Ti–O–P bonds, rather than forming polyphosphoric acid (PO_4^{3-}) entities attached to the surface of TiO_2.[45]

The UV-Vis spectra of the prepared samples are shown in Figure S6(b). Notably, it's evident from these spectra that P-doping significantly extends the wavelength sensitivity of TiO_2 into the visible light region. To determine the energy band gap (E_g), we employed Tauc's relation, involving the plot $(Fh\nu)^{0.5} = f(h\nu)$, where F represents the absorbance coefficient, and $h\nu$ is the photon energy. According to our calculations, the energy gap values for the non-doped, 2% phosphorus-doped, and 10% phosphorus-doped samples were 2.90 eV, 2.87 eV, and 2.75 eV, respectively.

To complement these experiments, we computed the partial density of states (PDOS) using DFT (Figure 1f–h) to analyze the effect of P-doping on the electronic band gap of TiO_2. We obtained a wide band gap (2.57 eV) in pristine TiO_2, whereas upon doping with 2% P, the band gap is reduced to 2.26 eV. Moreover, with 10% P-doping, the band gap is further reduced to 1.06 eV (spin up) and 2.11 eV (spin down). We note that the PBE functional tends to underestimate the band gap.[49,50] Hence, the inclusion of P appears to reduce the band gap in agreement with the experimental findings. Inspection of the PDOS suggest that in 10% P-doped TiO_2, the significant reduction in the band gap is due to additional Ti^{3+}-d states. However, no P^{5+}-3p states are observed near the Fermi level. The obtained results confirm that the phosphorus doping reduces the band gap and improves the electronic conductivity of TiO_2. The improved electronic conductivity may facilitate the transport and reaction between lithium ions and TiO_2 during the charge/discharge cycling, offering enhanced electrochemical properties.

To identify the electronic structure of the prepared materials, X-ray Absorption Near-edge Fine Structure (XANES) spectroscopy was carried out. As depicted in Figure 2(a), the XANES spectra of the Ti K-edge in non-doped and P-doped TiO_2 samples exhibit similar behavior. This similarity confirms that there is a comparable local structural modification of the Ti cations in all materials.[51,52] The weak intensity of the Ti pre-edge peak can be explained by the strong symmetry exhibited by the neighboring Ti cations in these materials.[53,54] The enhancement in the pre-edge peak intensity for the P-doped materials reflects the local structural and electronic structure perturbations caused by P insertion in the TiO_2 lattice. Moreover, the Ti K-edge peak at 4985.6 eV for P-doped TiO_2 samples shows a slightly lower intensity compared to the non-doped
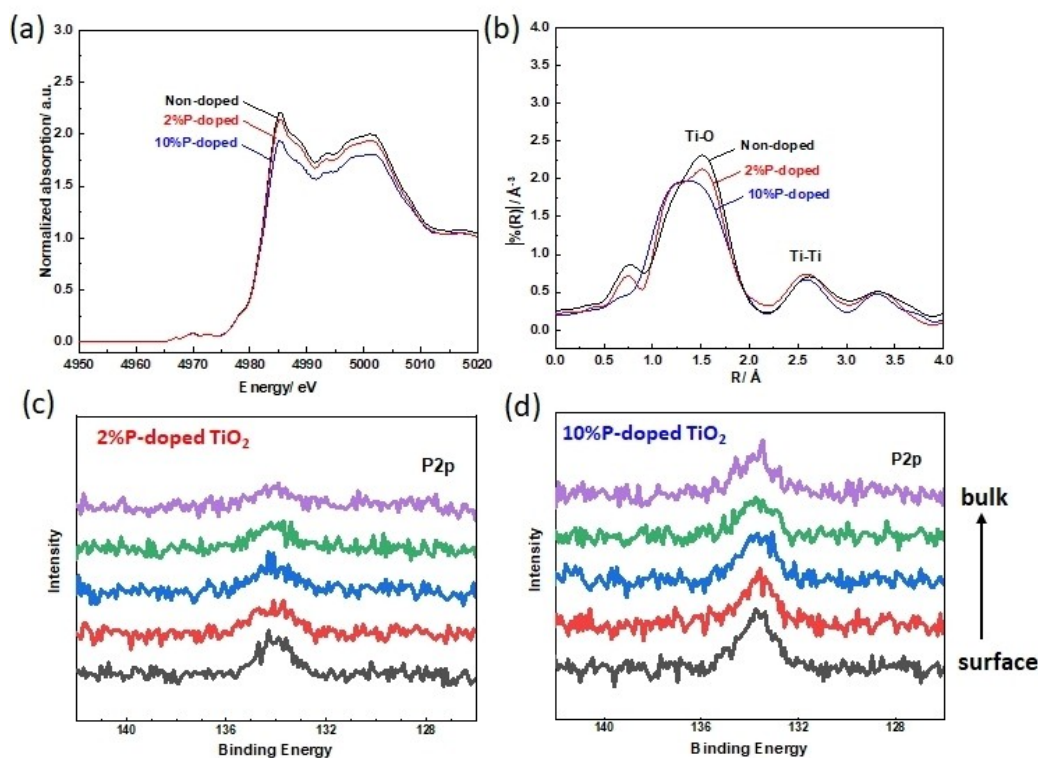
Figure 2. a) XANES spectra on Ti:K edge, b) Fourier transforms of the Ti:K edge EXAFS functions, and XPS depth profiling of c) 2%P-doped TiO_2 and d) 10%P-doped TiO_2.

Batteries & Supercaps

Research Article
doi.org/10.1002/batt.202300424

Chemistry
Europe

European Chemical
Societies Publishing

material (4985.3 eV), signifying that the Ti species undergo partial reduction after P-doping.

The bond length information of non-doped and 2%P-doped materials was investigated by the Fourier transformed (FT) of Ti K-edge Extended X-ray Absorption Fine Structure (EXAFS) spectra (Figure 2b). The non-doped and 2%P-doped TiO_2 show two peaks representing the Ti–O and Ti–Ti coordination shells, respectively.[52–54] Importantly, the phosphorus doping in TiO_2 structure results in a reduction of the Ti–O bond length, accompanied by a broader distribution, indicating that phosphorus cations are effectively integrated within the frame-work of TiO_2.[55]

XPS measurements were used to determine the oxidation state of the doped phosphorus in the prepared materials. Figure S7(a–d) depicts the P 2p XPS spectra of 2%P-doped and 10%P-doped TiO_2 samples. the P2p peak for the TiO_2 samples seems to include a P–O (PO_4) bond. Moreover, according to earlier reports and the fact that P^{5+} has an ionic radius of 0.38 and Ti^{4+} has a value of 0.67, we propose that P accesses Ti^{4+} sites as P^{5+} in the crystal lattice through the creation of Ti–O–P bonds.[56–58] Formation energy calculations obtained using DFT also suggest that P-ions reside at Ti-sites (Figure 1). Moreover, as illustrated by the XPS depth profiling (Figure 2c, d), 2%P-doped material shows a relatively uniform P distribution, with a low concentration of P in the bulk. This uniform distribution generally promotes good cycling stability, as the TiO_2 structure remains largely intact, and the P doping on the surface enhances lithium-ion mobility and improves charge-discharge kinetics. However, in 10%P-doped TiO_2 material, there is a higher concentration of P distributed throughout the bulk. This higher concentration of P in the bulk may disrupt the lattice structure of TiO_2, leading to structural degradation during cycling. This can result in irreversible capacity loss and diminished cycling stability.

The electron distribution along the Ti–O–P bond is perturbed by the partial substitution of Ti^{4+} with P^{5+}. This perturbation arises not only from differences in valence states but also from variations in the sizes of both ions. Computational results further validate this disturbance in the electronic structure. Hence, we suggest that electron transfer within the crystal lattice is feasible, given the observed charge accumulation around P in the Ti–O–P bonds. The observed redshift in the UV-vis reflectance absorption spectrum, as shown in Figure S6(b), could potentially be attributed to the formation of Ti–O–P bonds within the crystal lattice.

We also studied the effect of P-doping on oxygen binding in TiO_2. ICOHP results are shown for pristine and doped TiO_2 in Figure 3. Weak bonding is observed for Ti–P in Figure 3(d, e), as expected, since P substitutes at Ti sites. Additionally, consistent ICOHP values for Ti–O indicate that Ti–O bonding is not greatly affected by P-doping (Figure 3a–c), whereas O–P bonds have considerably more negative ICOHP values (Figure 3f, g). Hence, P-doping effectively binds oxygen in TiO_2.
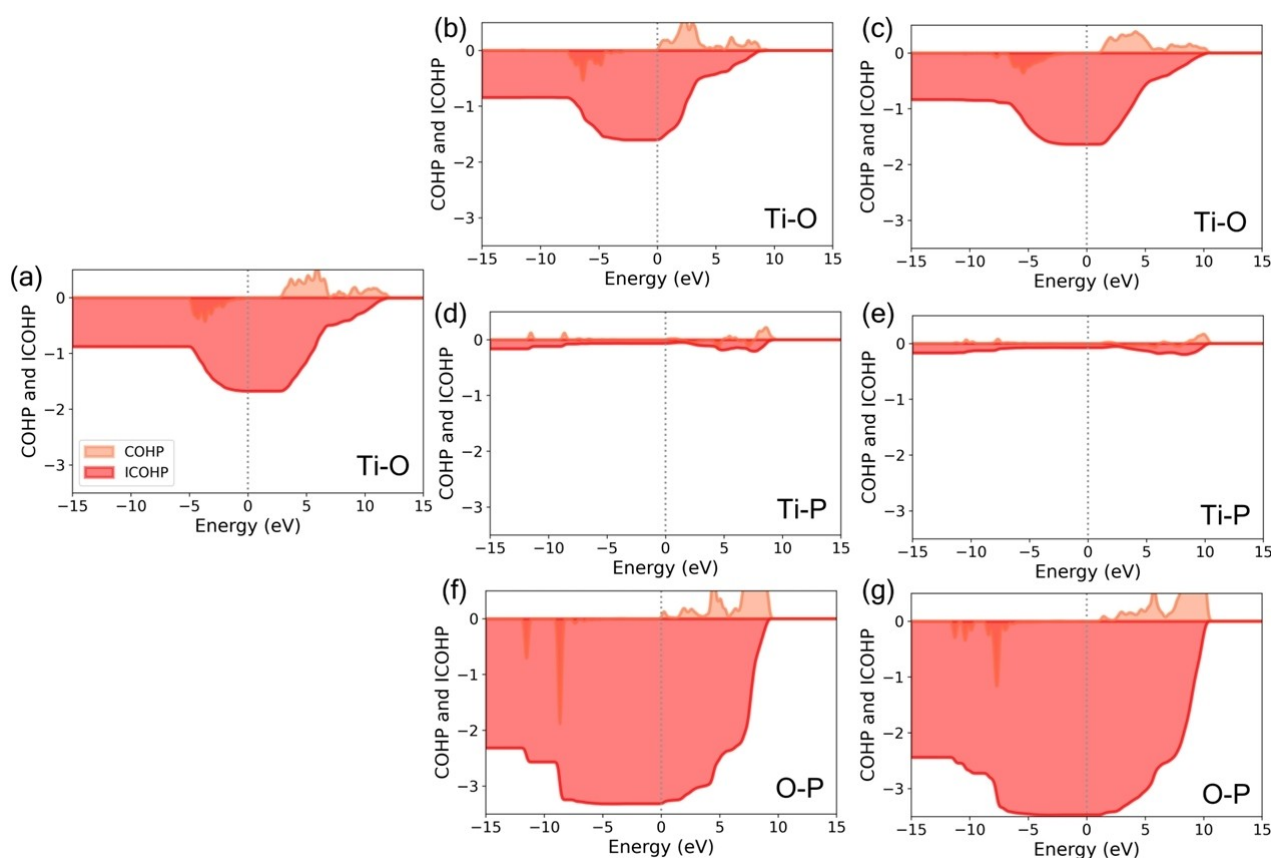
Figure 3. ICOHP results of a) non-doped, b, d, f) 2%P-doped and c, e, g) 10%P-doped TiO_2 materials calcined at 450 °C.

Batteries & Supercaps

Research Article
doi.org/10.1002/batt.202300424

Chemistry
Europe

European Chemical
Societies Publishing

Electrochemical characterizations

For the electrochemical measurements, cycling was carried out at 0.1 C (1 C = 336 mA g^{-1}) within the voltage range of 1.0–3.0 V. The discharge/charge curves of non-doped and P-doped electrodes are illustrated in Figure 4(a). As it can be seen for all materials, the discharge/charge curves have two plateaus at 1.9 V and 1.7 V representing lithiation/delithiation of anatase TiO$_2$, respectively. In addition, excellent first coulombic efficiencies of 99% and low hysteresis have been shown for P-doped electrodes compared to the non-doped electrode. This superior performance could be attributed to the enhanced electronic conductivity of the P-doped samples, as demonstrated by PDOS study and UV-Vis spectroscopy.

The lithiation/delithiaiton properties of the prepared electrodes were studied using Cyclic Voltammetry technique in the voltage window of 1.0 and 3.0 V and a scanning speed of 0.05 mV s^{-1}. Figure 4(b) shows the presence of cathodic and anodic peaks at 1.7 and 1.9 V, respectively, which can be attributed to the lithiation/delithiaiton of TiO$_2$ anatase nanoparticles. The cathodic/anodic peaks confirm the result obtained by the galvanostatic discharge/charge tests. Besides, CV multi-rates (from 0.05 to 1 mV s^{-1}) (Figure S8) were carried out to calculate the diffusion coefficients of lithium ions in the three
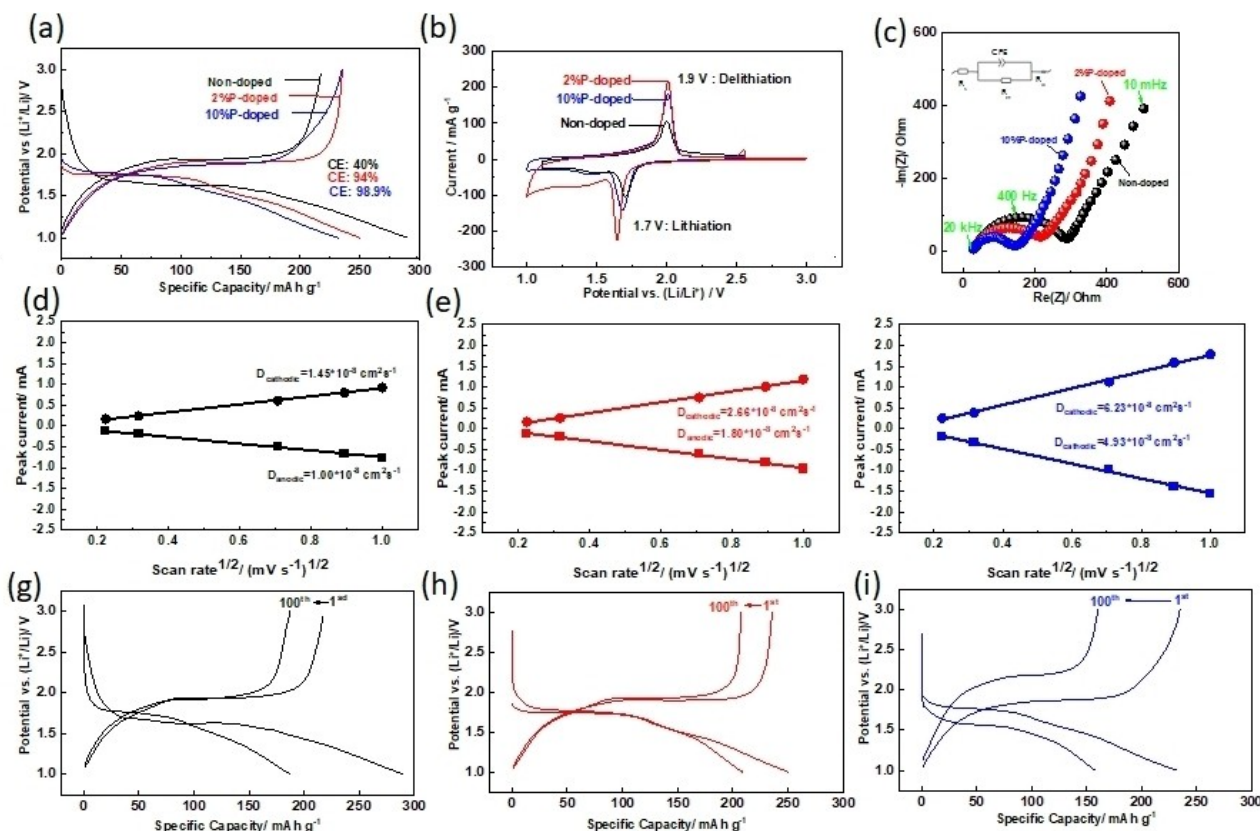
electrodes. For this purpose, the Randles-Sevcik equation was used [Equation (1)]:

$$I_p = 2.69 \times 10^5 \, A \, n^{3/2} \, C_0 \, D^{1/2} \, v^{1/2} \tag{1}$$

where I_p is the peak current (mA), A is the electrode surface area (cm^2), n is the number of exchanged electrons (for Li$^+$ it is 1), C_0 is the change of Li concentration associated with the specific electrochemical reaction. This change is 2.34×10^{-2} mol cm^{-3} when $x = 0.5$, calculated based on the volume of TiO$_2$ (142.02 Å^3). v is the scan rate (mV s^{-1}) and D is the diffusion coefficient (cm^2 s^{-1}). According to the results displayed in Figure 4(d–f), the calculated diffusion coefficients of the prepared materials are summarized in Table 3.

Table 3. Anodic and cathodic diffusion coefficient of the prepared materials.

	Anodic diffusion coefficient [cm^2 s^{-1}]	Cathodic diffusion coefficient [cm^2 s^{-1}]
Non-doped	1.00×10^{-8}	1.45×10^{-8}
2%P-doped	1.80×10^{-8}	2.66×10^{-8}
10%P-doped	4.93×10^{-8}	6.23×10^{-8}

Figure 4. a) First charge/discharge cycle of non-doped TiO$_2$ and P-doped TiO$_2$ materials cycled at 0.1 C. b) Cyclic voltammograms of the first cycle scanned at 0.05 mV s^{-1}. c) Nyquist plot of non-doped TiO$_2$ and P-doped TiO$_2$ materials. d–f) Anodic and cathodic peak current versus square root of scan rate of d) non-doped, e) 2%P-doped, and f) 10%P-doped TiO$_2$, and g–i) Galvanostatic discharge/charge cycles of g) non-doped, h) 2%P-doped and i) 10%P-doped TiO$_2$ electrodes after 100 cycles at 0.1 C.

The observed highest diffusion coefficient of lithium ions in the P-doped materials is attributed to the beneficial effects of enhanced electronic conductivity (Figure S6b) and the creation of ionic channels through doping. These effects, when combined, synergistically enhance the movement of both electrons and lithium ions, ultimately leading to improved coulombic efficiency and overall performance of the battery.

Electrochemical impedance spectroscopy (EIS) was used in a frequency range from 10 mHz to 10 MHz to understand the electrode kinetics. As shown in Figure 4(c), In the high-frequency region of the Nyquist plots, a semicircular pattern is evident, while a linear slope characterizes the low-frequency region. This result suggests that both charge transfer and lithium-ion diffusion control the electrochemical behavior.[59,60] Importantly, according to the modified Randles equivalent circuit shown in the inset of Figure 4(c), the charge-transfer resistance at the electrode/electrolyte interface (R_{ct}) of 2% and 10%P-doped TiO$_2$ electrodes are 187 Ω and 99 Ω, respectively, which is much lower than that of non-doped TiO$_2$ electrodes (257 Ω). Moreover, the bulk resistance of the electrolyte, separator, and electrode (R_s) of 2% and 10%P-doped TiO$_2$ electrodes are also lower than that of non-doped TiO$_2$ material (29 Ω) as shown in Table 4 indicating the better electronic and ionic conductivity of the doped TiO$_2$ electrodes. In fact, the substitution of Ti ions with P ions might create Ti vacancies, O vacancies, or conduction band electrons to balance the charge,[61,62] Thus, the material's electrical conductivity is greatly increased, resulting in less internal resistance and easier charge transfer. This result agrees with the UV-V, PDOS and Cyclic voltammetry multi-rate results.

Figure S9 shows the long-term cycling at 0.1 C rate (1 C = 336 mA g^{-1}) for 100 cycles. The P-doped electrodes demonstrate an improved reversible discharge capacities of 235 mAh g^{-1}, compared to 218 mAh g^{-1} for the non-doped TiO$_2$. This outcome can be attributed to the enhanced electronic conductivity and lithium-ion diffusion coefficient of P-doped electrodes. However, it is interesting to note that the 2%P-doped electrode maintains its performance after 100 cycles at 0.1 C, while the 10%P-doped electrode exhibits more hysteresis and lower

discharge capacities (160 mAh g^{-1}) after the same number of cycles. This observation is corroborated by the results depicted in Figure 4(g–i). Specifically, the 2%P-doped TiO$_2$ electrode displays an improved capacity retention of 83% after 100 cycles at 0.1 C, in contrast to the 10%P-doped TiO$_2$ electrode, which only achieves a capacity retention of 67% (Table 5). These results prove that the highest concentration of phosphorus doping might create structural defects in the TiO$_2$ material and hence decrease its electrochemical performance during prolonged cycling.

The rate capability profiles at various current rates ranging from 0.1 C to 10 C within the voltage range of 1.0–3.0 V are displayed in Figure S10. The non-doped TiO$_2$ demonstrate a reversible capacity of 200 mAh g^{-1} at 0.1 C. At 1 C, the reversible capacity remains higher than 145 mAh g^{-1}. However, for P-doped TiO$_2$ electrodes, the reversible capacity reached 230 mAh g^{-1} at 0.1 C current rate and 175 mAh g^{-1} at 1 C. The capacity was restored to 185 mAh g^{-1} at 0.1 C rate for non-doped electrode and to 210 mAh g^{-1} and 225 mAh g^{-1} for 2%P-doped and 10%P-doped TiO$_2$, respectively. This result shows the high stability of the anatase TiO$_2$ electrodes and confirms the beneficial effect of P-doping on TiO$_2$ material. Table S1 summarizes the different synthesis methods and the reversible capacity of various doped TiO$_2$ based negative electrode for lithium-ion batteries reported in the literature. The electrodes based on our synthesis method delivers similar or even superior performances to several reported works with complicated synthesis methods.

XAS Spectroscopy was carried out for non-doped, 2%P-doped and 10%P-doped TiO$_2$ electrodes after the first cycle at 0.1 C in a voltage range of 1–3 V (vs. Li$^+$/Li) and the results are depicted in Figure 5. As shown in Figure 5(a), the pre-edge and edge characteristics peaks are all very similar to non-cycled electrodes, with only minor changes in the peak's intensity. Due to the minimal information given by XANES spectra, we focused on the Fourier transforms of the Ti:K edge EXAFS functions, which contains information on local structure. Figure 5(b and c) depicts the EXAFS signal of P-doped and non-doped TiO$_2$ electrodes after one charge/discharge cycle. At the end of delithiation, the non-doped TiO$_2$ material shows an important structural disorder and a change in interatomic distances, which is reflected in the lower intensity of Fourier transforms spectra. Moreover, the Ti valence of the doped materials at the end of delithiation is similar to the non-cycled materials suggesting their high reversibility upon lithium insertion/disinsertion compared to the non-doped material. This result confirms the results obtained form charge/discharge tests which proved the high first coulombic efficiency for the doped materials.

Table 4. Independent resistive components of the non-doped, 2%P-doped and 10%P-doped electrodes using an equivalent circuit.

Electrode	R_s [Ω]	R_{ct} [Ω]
Non-doped	29	257
2%P-doped	25	187
10%P-doped	17	99

**Table 5.** Discharge capacity, columbic efficiency, and capacity retention of the prepared materials.

	Cycle 1		Cycle 100		
	Discharge capacity	Columbic efficiency	Discharge capacity	Columbic efficiency	Capacity retention
Non-doped	290	40	187	99.8	65
2%P-doped	250	94	209	99.4	85
10%P-doped	237	99	160	99.1	67
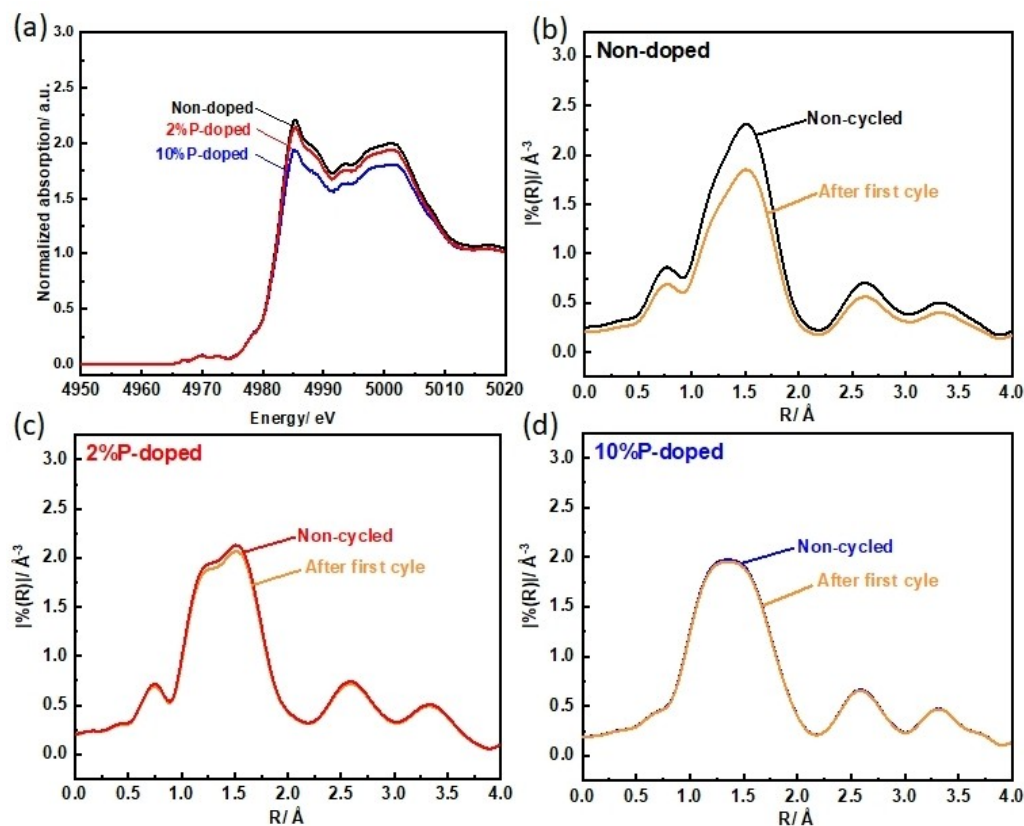
Figure 5. a) XANES spectra on Ti:K edge and b–d) Fourier transforms of the Ti:K edge EXAFS functions for non-doped, 2%P-doped and 10%P-doped TiO$_2$ materials after the first cycle at 0,1 C in a voltage range 1–3 V.

In order to get further information of the lithiation reaction mechanism and the structural evolution of the prepared materials, the two first charge-discharge cycles were inves-tigated using operando XRD (Figure 6). At the Open Circuit Voltage (OCV) state, only the two characteristic peaks (101) and (004) of the anatase TiO$_2$ phase are visible in the diffraction
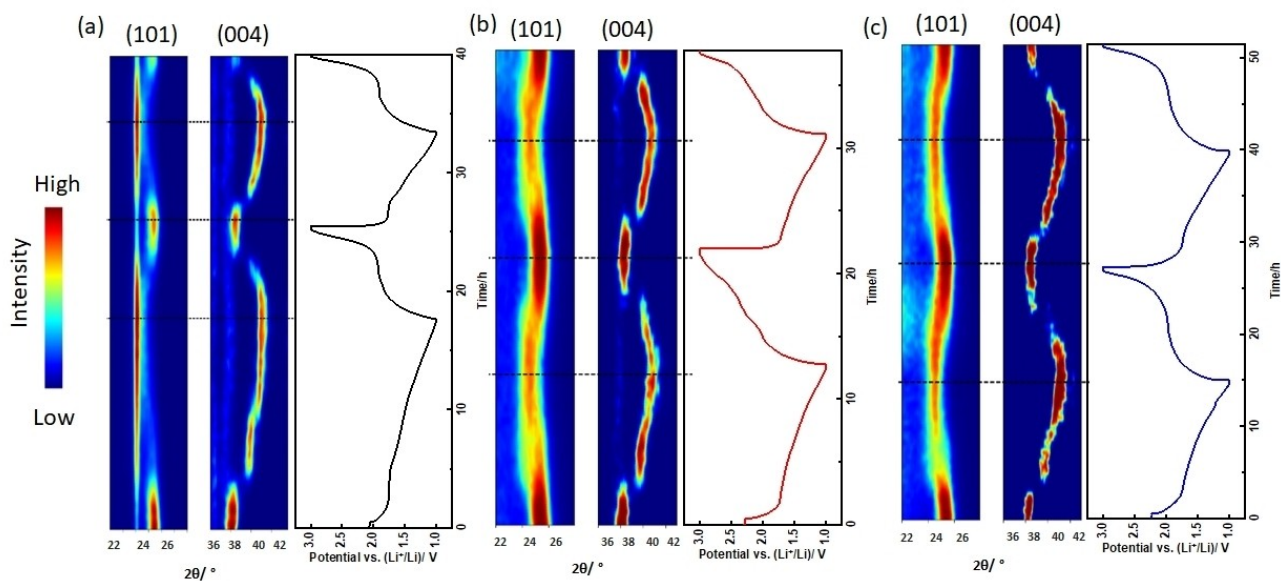
Figure 6. Operando XRD patterns and discharge/charge galvanostatic data at 0.05 C current rate of a) non-doped, b) 2%P-doped and c) 10%P-doped TiO$_2$ electrodes during the two first cycles.

Batteries & Supercaps

Research Article
doi.org/10.1002/batt.202300424

Chemistry Europe

European Chemical
Societies Publishing

patterns at 25.4° and 38.1°, respectively. During the first discharge, the intensities of these peaks show a gradual decrease without the appearance of any new peaks in the diffraction pattern. This decrease continues until the peaks completely disappears at the end of the small plateau at 1.7 V (versus Li/Li$^+$). The diffraction peaks for all materials show a significant shift to greater angles, indicating the incorporation of lithium ions in TiO_2. Furthermore, the diffraction peaks gradually revert to smaller angles during the charge, which corresponds to the extraction of lithium ions from TiO_2. Comparing the reversibility of lithium intercalation/deintercalation, it is clearly observed that the reversibility increases by increasing the concentration of P doping confirming the results obtained by XAS spectroscopy of the cycled electrodes. The result obtained by Operando XRD demonstrates that the TiO_2 electrodes' crystallinity was preserved during the lithiation/delithiation process. The good structural stability of anatase TiO_2 materials should be explained by our synthesis method based on biopolymers gelation.[63]

Despite the various works done on TiO_2 as anode for lithium-ion batteries (regardless of the synthesis routes), no extensive results are available on the electrochemical performance of such anodes in full-cells, and most of the research reported on TiO_2 anodes are limited to half-cell configuration. In this work, a full cell was designed using 2%P-doped TiO_2 anode and LFP as cathode. Figure 7(a) shows the first three Charge/Discharge cycles of 2%P-doped TiO_2/ LFP full cell at 0.1 C (1 C = 170 mA g^{-1}) in a voltage range of 1.0–2.5 V. In the first cycle, the full cell delivers a capacity of 148 mAh g^{-1} (based on the mass of LFP). Moreover, the dq/dv peaks depicted in Figure 7(b) shows that the full cell potential is 1.6 V matching the voltage

difference between 2%P-doped TiO_2 and LFP. Based on this voltage, the energy density of the full cell was estimated to be 112 Wh kg^{-1}. In addition, the 2%P-doped TiO_2/LFP full cell delivers excellent rate capabilities at different C-rates (Figure 7c). It provides a discharge capacity of 105 mAh g^{-1} at 1 C and even at 5 C, the battery still delivers a capacity of 40 mAh g^{-1}. Eventually, we studied the cycling performance of the full cell (Figure 7d). After 1000 cycles a capacity retention of 96% was observed at 1 C with a columbic efficiency of 100% for 2%P-doped TiO_2/ LFP full cell. However, the non-doped TiO_2/LFP full cell retains only 36% of its initial capacity which does not exceed 74 mAh g^{-1}. The low capacity as well as capacity retention of the non-doped TiO_2/LFP full cell can be explained by the low first columbic efficiency of non-doped TiO_2 anode which causes a capacity loss of 75 mAh g^{-1} during the first cycle. The effectiveness of phosphorus doping in enhancing the first columbic efficiency of TiO_2 makes it a promising strategy for the development of high-performance lithium-ion batteries with improved cycling stability and energy storage capabilities.

Conclusions

In summary, non-doped and P-doped TiO_2 materials have been successfully prepared by Sol-Gel method using sodium alginate biopolymer as complexing agent. Structural, morphological, textural characteristics and lithium insertion mechanism of P-doped TiO_2 materials have been carefully studied and compared to non-doped material. The results of the electrochemical tests indicate that 2%P-doped TiO_2 material has the optimal
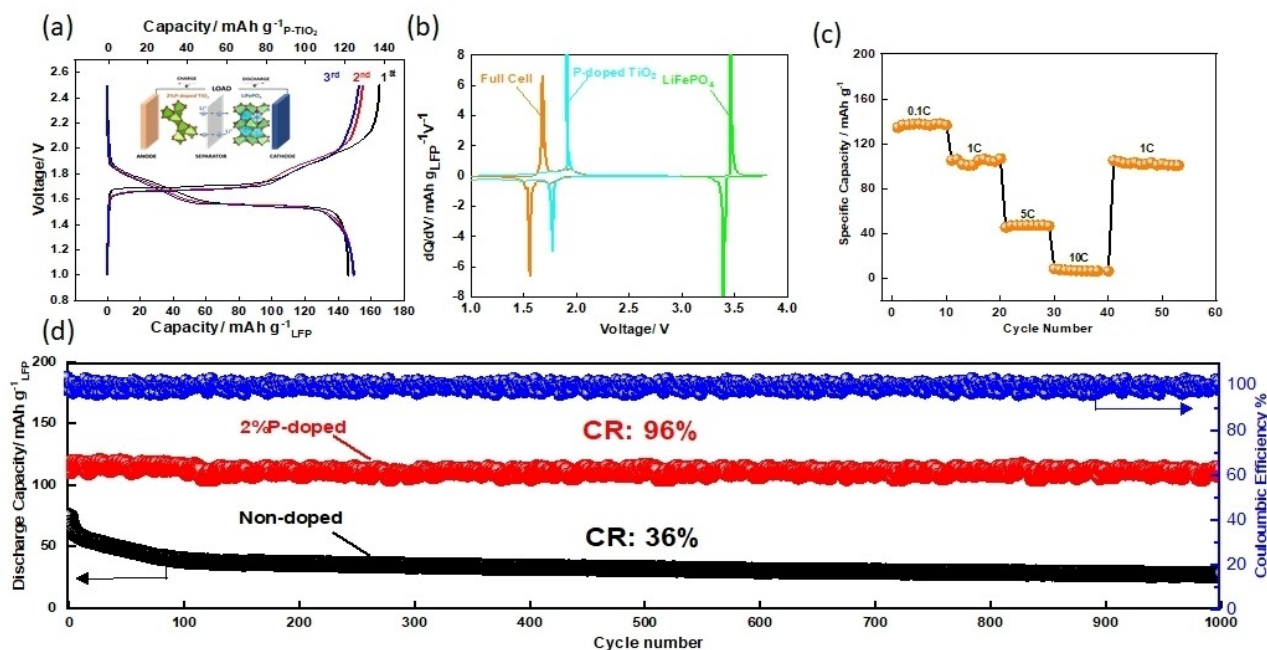
Figure 7. a) Three first charge/discharge cycles of the LiFePO$_4$/2%P-doped TiO$_2$ lithium-ion cell performed at 0.1 C rate (1 C = 170 mA g^{-1}) within the voltage range of 1–2.5 V (inset: schematic illustration of the Full Cell), b) dq/dv peaks, c) rate performance at different rates, d) cycling performances at 1 C charge/discharge rate.

Batteries & Supercaps

Research Article
doi.org/10.1002/batt.202300424

Chemistry Europe
European Chemical
Societies Publishing

performance. The improved electrochemical performance after P doping can be attributed to the band gap changes after doping proved by UV-Vis measurement and PDOS study, the high lithium diffusion proved by Cyclic Voltammetry multi-rate, the low polarization proved by impedance spectroscopy and the high lithium insertion/disinsertion reversibility confirmed by XAS spectroscopy and Operando XRD. These results prove the beneficial effect of phosphorus doping to improve the electronic conductivity and dynamic property of anatase TiO_2 material and therefore improves its reversibility during prolonged cycles. Furthermore, a high-performance full lithium-ion battery was designed using 2 %P-doped TiO_2 anode and LiFePO$_4$ cathode. The output voltage was about 1.6 V with a high initial specific capacity of 148 mAh g^{-1} at 0.1 C, high rate-capability and high-capacity retention of 96 % after 1000 cycles at 1 C. Taking into consideration the low cost, abundancy, high safety, and environmental friendliness of P-doped TiO_2 and LiFePO$_4$, this work demonstrates the practical application of P-doped TiO_2 and LiFePO$_4$ as cost-effective and highly safe electrodes materials for future lithium-ion batteries.

Experimental Section

Materials

The P-doped TiO_2 nanoparticles were synthesized via a simple sol gel method. Typically, Titanium (IV) TetraIsoPropoxide (TTiP, 99.999 %, Sigma Aldrich) was added dropwise into Ethanol (CH_3CH_2OH, pure, Sigma Aldrich) under stirring. Then, sodium alginate polymer (($C_6H_7O_6Na)_n$, Sigma Aldrich) was used in the form of solution. This solution was obtained by directly dissolving sodium alginate powder in distilled water under strong stirring. A white suspension was obtained by adding dropwise the sodium alginate solution and phosphoric acid (H_3PO_4, 85 %, Sigma Aldrich) (P-dopant to Ti ratios of 0, 2, and 10 mol% in the TiO_2 samples) to the Titanium (IV) TetraIsoPropoxide solution. After being collected by centrifugation, washed with distilled water several times, the resulting powder was dried at 70 °C and calcined at 450 °C for 4 h in air. The synthesis conditions are shown in Figure S1.

Electrodes preparation and cells assembly

The preparation of the working electrodes involved mixing the active material, Carbon Black (CB, Sigma Aldrich), and Polyvinylidene fluoride (PVDF, Sigma Aldrich) in a weight ratio of 7:2:1. The mixture was dissolved in N-methyl-2-pyrrolidone (NMP, 99.5 %, Sigma Aldrich) to obtain a homogenous slurry. This slurry was coated on a Copper foil using Dr. blade technique and dried at 80 °C for 5 hours. The coin cells were assembled in an Ar-filled glovebox employing lithium foil or LFP (full cell) as counter electrodes, Celgard 2400 film as separator and 1 M LiPF$_6$ in EC-DEC as electrolyte. The LFP electrode, 85 wt% LFP, 10 wt% Carbon Black and 5 wt% PVDF coated on aluminum foil, was used as cathode on the full cell. The anode is in slight excess over the cathode, and the specific capacity is determined using the mass of LFP.

Characterizations

After the synthesis of TiO_2 and P-doped TiO_2 materials, crystal structure, morphology and surface area were characterized using X-ray diffraction (XRD, BRUKER D8 ADVANCE diffractometer, with Cu K_α radiation) and Raman Spectroscopy (LabRAM 300 Raman spectrometer - Horiba Jobin Yvon), Scanning Electron Microscopy (ZEISS EVO 10 microscope) and Brunauer, Emmett & Teller (BET, Micromeritics Gemini VII), respectively. Additionally, chemical bonding and absorbance properties of TiO_2 materials were identified using Fourier transform infrared spectroscopy (FTIR, PerkinElmer Spectrometer) and Ultraviolet-Visible Spectrophotometry (UV-V, PerkinElmer Spectrophotometer). Besides, X-ray absorption spectroscopy (XAS) and X-ray photoelectron spectrometry (XPS) have been carried out in the Argonne national laboratory to identify the electronic structure as well as the oxidation state of the doped phosphorus in the prepared materials.

For the electrochemical tests, cyclic voltammetry (CV) was employed within the voltage range of 1–3 V at different scan rates from 0.05 to 1 mV s^{-1}. In addition, galvanostatic charge/discharge cycling, Electrochemical impedance spectroscopy (EIS) in a frequency range from 10 mHz to 10 MHz, Rate capability, Operando XRD and Ex-situ XAS in the voltage window of 1–3 V were performed using MPG-2, Bio-Logic SAS potentiostat.

Computational methodology

All DFT calculations were performed using the generalized gradient approximation Perdew-Burke-Ernzerhof (GGA-PBE)[64] exchange-correlation functional as implemented in the Vienna ab initio simulation package (VASP).[64,65] A Hubbard-U parameter (4.2 eV)[66] for Ti-d state interactions was employed to account for Coulomb corrections.[67] To represent the core electrons, projector-augmented-wave (PAW) potentials[68] were used and a kinetic energy cutoff of 600 eV was used for the plane-wave basis set. Brillouin zone sampling was performed using the Monkhorst-Pack grid[69] with a k-points mesh of 4×4×2 centered at the Γ-point. A supercell of 3×3×1 with 36 Ti atoms and 72 O atoms was considered for geometry optimizations. For structural relaxation and self-consistency, the convergence values for the energy and forces were set to 10^{-6} eV/unit cell and 0.01 eV/Å per atom, respectively. To identify suitable dopant sites for P-ions in the TiO_2 crystal, the Monte Carlo simulated annealing (MCSA) technique[44] based on classical force field (FF) was employed using a locally modified version of the GULP code.[42–44] Both Ti and O sites were considered for swapping within the MCSA scheme. In MCSA simulations, Coulomb and Buckingham potentials were used to calculate the FF potential energy surface. The lowest energy structure was further considered for density functional theory (DFT) optimizations. To understand the impact of doping chemical bonding, the bond strength of Ti—O, Ti—P and O—P was studied using the crystal orbital Hamiltonian population method (COHP) and its integrated version (ICOHP), which are implemented in the Lobster code.[70–72] For COHP and ICOHP calculations, bond distances were considered to be in the range 1.0 to 3.0 Å for Ti—O and O—P while 1.0 to 4.5 Å for Ti—P due to greater bond length.

Supporting Information

The authors have cited additional references within the Supporting Information.[73–83]

Batteries & Supercaps

Research Article
doi.org/10.1002/batt.202300424

Chemistry
Europe

European Chemical
Societies Publishing

Conflict of Interests

The authors declare no conflict of interest.

Data Availability Statement

The data that support the findings of this study are available from the corresponding author upon reasonable request.

[1] Y. Zheng, B. Liu, P. Cao, H. Huang, J. Zhang, G. Zhou, *J. Mater. Sci. Technol.* **2019**, *35*, 667.

[2] S. Wang, C. Qu, J. Wen, C. Wang, X. Ma, Y. Yang, G. Huang, H. Sun, S. Xu, *Mater. Chem. Front.* **2023**.

[3] Y. Chen, X. Chen, Y. Zhang, *Energy Fuels* **2021**, *35*, 6420.

[4] S. Qiu, L. Xiao, X. Ai, H. Yang, Y. Cao, *ACS Appl. Mater. Interfaces* **2017**, *9*, 345.

[5] B. Guo, K. Yu, H. Fu, Q. Hua, R. Qi, H. Li, H. Song, S. Guo, Z. Zhu, *J. Mater. Chem. A* **2015**, *3*, 6392.

[6] Z. Liu, Q. Yu, Y. Zhao, R. He, M. Xu, S. Feng, S. Li, L. Zhou, L. Mai, *Chem. Soc. Rev.* **2019**, *48*, 285.

[7] P. Guan, J. Li, T. Lu, T. Guan, Z. Ma, Z. Peng, X. Zhu, L. Zhang, *ACS Appl. Mater. Interfaces* **2018**, *10*, 34283.

[8] C. Shen, X. Fang, M. Ge, A. Zhang, Y. Liu, Y. Ma, M. Mecklenburg, X. Nie, C. Zhou, *ACS Nano* **2018**, *12*, 6280.

[9] N. Liu, J. Liu, D. Jia, Y. Huang, J. Luo, X. Mamat, Y. Yu, Y. Dong, G. Hu, *Energy Storage Mater.* **2019**, *18*, 165.

[10] M. Furquan, A. Raj Khatribail, S. Vijayalakshmi, S. Mitra, *J. Power Sources* **2018**, *382*, 56.

[11] T. Mu, P. Zuo, S. Lou, Q. Pan, Q. Li, C. Du, Y. Gao, X. Cheng, Y. Ma, G. Yin, *Chem. Eng. J.* **2018**, *341*, 37.

[12] M. Armand, J.-M. Tarascon, *Nature* **2008**, *451*, 652.

[13] Y.-J. Han, J. Kim, J.-S. Yeo, J. C. An, I.-P. Hong, K. Nakabayashi, J. Miyawaki, J.-D. Jung, S.-H. Yoon, *Carbon* **2015**, *94*, 432.

[14] X. Yan, F. Jiang, X. Sun, R. Du, M. Zhang, L. Kang, Q. Han, W. Du, D. You, Y. Zhou, *J. Alloys Compd.* **2020**, *822*, 153719.

[15] Jiang, Yan, Du, Kang, Du, Sun, Zhou, *Nanomaterials* **2019**, *9*, 996.

[16] B. Scrosati, J. Garche, *J. Power Sources* **2010**, *195*, 2419.

[17] H. Kim, W. Choi, J. Yoon, J. H. Um, W. Lee, J. Kim, J. Cabana, W.-S. Yoon, *Chem. Rev.* **2020**, *120*, 6934.

[18] H. Qiao, Y. Wang, L. Xiao, L. Zhang, *Electrochem. Commun.* **2008**, *10*, 1280.

[19] B. Dunn, H. Kamath, J.-M. Tarascon, *Science* **2011**, *334*, 928.

[20] Z. Wang, F. Zhang, H. Xing, M. Gu, J. An, B. Zhai, Q. An, C. Yu, G. Li, *Electrochim. Acta* **2017**, *243*, 112.

[21] Z. Jin, M. Yang, J. Wang, H. Gao, Y. Lu, G. Wang, *Chem. A Eur. J.* **2016**, *22*, 6031.

[22] X. Wang, Q. Meng, Y. Wang, H. Liang, Z. Bai, K. Wang, X. Lou, B. Cai, L. Yang, *Appl. Energy* **2016**, *175*, 488.

[23] S. Yuan, Q. Lai, X. Duan, Q. Wang, *J. Energy Storage* **2023**, *61*, 106716.

[24] Y. Wu, Y. F. Yuan, F. Chen, M. Zhu, G. C. Cai, S. M. Yin, J. L. Yang, S. Y. Guo, *Mater. Lett.* **2019**, *240*, 96.

[25] W. Wang, M. Wu, P. Han, Y. Liu, L. He, Q. Huang, J. Wang, W. Yan, L. Fu, Y. Wu, *ACS Appl. Mater. Interfaces* **2019**, *11*, 3061.

[26] Y. Cai, H.-E. Wang, J. Jin, S.-Z. Huang, Y. Yu, Y. Li, S.-P. Feng, B.-L. Su, *Chem. Eng. J.* **2015**, *281*, 844.

[27] J. Jin, S.-Z. Huang, J. Shu, H.-E. Wang, Y. Li, Y. Yu, L.-H. Chen, B.-J. Wang, B.-L. Su, *Nano Energy* **2015**, *16*, 339.

[28] Y.-M. Jiang, K.-X. Wang, H.-J. Zhang, X.-X. Guo, J.-F. Wang, G.-D. Li, J.-S. Chen, *RSC Adv.* **2013**, *3*, 26052.

[29] J. Wei, J. X. Liu, Y. C. Dang, K. Xu, Y. Zhou, *Adv. Mater. Res.* **2013**, *750–752*, 301.

[30] X. Wang, Z. Jia, F. Liu, H. Liang, X. You, K. Wang, X. Lou, W. Shuang, L. Xiao, B. Cai, L. Yang, *RSC Adv.* **2016**, *6*, 48985.

[31] F. He, F. Ma, J. Li, T. Li, G. Li, *Ceram. Int.* **2014**, *40*, 6441.

[32] Y.-G. Guo, Y.-S. Hu, W. Sigle, J. Maier, *Adv. Mater.* **2007**, *19*, 2087.

[33] L. He, C. Wang, X. Yao, R. Ma, H. Wang, P. Chen, K. Zhang, *Carbon* **2014**, *75*, 345.

[34] B.-L. He, B. Dong, H.-L. Li, *Electrochem. Commun.* **2007**, *9*, 425.

[35] L. Cheng, D. Qiao, P. Zhao, Y. He, W. Sun, H. Yu, Z. Jiao, *Electrochim. Acta* **2019**, *300*, 417.

[36] N. El Halya, K. Elouardi, A. Chari, A. El Bouari, J. Alami, M. Dahbi, in *Titanium Dioxide – Advances and Applications*, IntechOpen, **2022**.

[37] W. Zhang, N. Luo, S. Huang, N.-L. Wu, M. Wei, *ACS Appl. Energ. Mater.* **2019**, *2*, 3791.

[38] J. Zheng, L. Liu, G. Ji, Q. Yang, L. Zheng, J. Zhang, *ACS Appl. Mater. Interfaces* **2016**, *8*, 20074.

[39] X. Wang, L. Qi, H. Wang, *ACS Appl. Mater. Interfaces* **2019**, *11*, 30453.

[40] X. Fan, T. Yu, Y. Wang, J. Zheng, L. Gao, Z. Li, J. Ye, Z. Zou, *Appl. Surf. Sci.* **2008**, *254*, 5191.

[41] K. El Ouardi, M. Dahbi, C. Hakim, M. O. Güler, H. Akbulut, A. El Bouari, I. Saadoune, *J. Appl. Electrochem.* **2020**, *50*, 583.

[42] J. D. Gale, A. L. Rohl, *Mol. Simul.* **2003**, *29*, 291.

[43] J. D. Gale, *J. Chem. Soc. Faraday Trans.* **1997**, *93*, 629.

[44] S. Kunnikuruvan, A. Chakraborty, D. T. Major, *J. Phys. Chem. C* **2020**, *124*, 27366.

[45] J. Wang, Y. Zhou, B. Xiong, Y. Zhao, X. Huang, Z. Shao, *Electrochim. Acta* **2013**, *88*, 847.

[46] J.-H. Jeong, D. Jung, E. W. Shin, E.-S. Oh, *J. Alloys Compd.* **2014**, *604*, 226.

[47] Y. Xia, Y. Jiang, F. Li, M. Xia, B. Xue, Y. Li, *Appl. Surf. Sci.* **2014**, *289*, 306.

[48] A. Bhaumik, S. Inagaki, *J. Am. Chem. Soc.* **2001**, *123*, 691.

[49] J. P. Perdew, M. Levy, *Phys. Rev. Lett.* **1983**, *51*, 1884.

[50] L. J. Sham, M. Schlüter, *Phys. Rev. Lett.* **1983**, *51*, 1888.

[51] L. Vallez, S. Jimenez-Villegas, A. T. Garcia-Esparza, Y. Jiang, S. Park, Q. Wu, T. M. Gill, D. Sokaras, S. Siahrostami, X. Zheng, *Energy Adv.* **2022**, *1*, 357.

[52] V. Bhasin, K. K. Halankar, A. Biswas, S. K. Ghosh, S. K. Sarkar, S. N. Jha, D. Bhattacharyya, *J. Alloys Compd.* **2023**, *942*, 169118.

[53] Y. Zhu, J. Li, C.-L. Dong, J. Ren, Y.-C. Huang, D. Zhao, R. Cai, D. Wei, X. Yang, C. Lv, W. Theis, Y. Bu, W. Han, S. Shen, D. Yang, *Appl. Catal. B* **2019**, *255*, 117764.

[54] R. G. Haverkamp, P. Kappen, K. H. Sizeland, K. S. Wallwork, *ACS Omega* **2022**, *7*, 28258.

[55] M. Sahoo, A. K. Yadav, S. N. Jha, D. Bhattacharyya, T. Mathews, N. K. Sahoo, S. Dash, A. K. Tyagi, *J. Phys. Chem. C* **2015**, *119*, 17640.

[56] S. P. Madhusudanan, B. Gangaja, A. G. Shyla, A. S. Nair, S. V. Nair, D. Santhanagopalan, *ACS Sustainable Chem. Eng.* **2017**, *5*, 2393.

[57] Q. Gan, H. He, Y. Zhu, Z. Wang, N. Qin, S. Gu, Z. Li, W. Luo, Z. Lu, *ACS Nano* **2019**, *13*, 9247.

[58] Z. Li, Y. Xin, W. Wu, B. Fu, Z. Zhang, *ACS Appl. Mater. Interfaces* **2016**, *8*, 30972.

[59] R. Mo, Z. Lei, K. Sun, D. Rooney, *Adv. Mater.* **2014**, *26*, 2084.

[60] H. Manjunatha, K. C. Mahesh, G. S. Suresh, T. V. Venkatesha, *Electrochim. Acta* **2011**, *56*, 1439.

[61] H. Bi, S. Zhu, Y. Liang, H. Jiang, Z. Li, S. Wu, H. Wei, C. Chang, H. Wang, Z. Cui, *ACS Omega* **2023**, *8*, 5893.

[62] J. A. Quirk, V. K. Lazarov, K. P. McKenna, *J. Phys. Chem. C* **2020**, *124*, 23637.

[63] K. El Ouardi, M. Dahbi, C. Hakim, M. O. Güler, H. Akbulut, A. El Bouari, I. Saadoune, *J. Appl. Electrochem.* **2020**, *50*, 583.

[64] J. P. Perdew, K. Burke, M. Ernzerhof, *Phys. Rev. Lett.* **1996**, *77*, 3865.

[65] G. Kresse, J. Furthmüller, *Comput. Mater. Sci.* **1996**, *6*, 15.

[66] S. L. Dudarev, G. A. Botton, S. Y. Savrasov, C. J. Humphreys, A. P. Sutton, *Phys. Rev. B* **1998**, *57*, 1505.

Batteries & Supercaps

Research Article
doi.org/10.1002/batt.202300424

Chemistry Europe
European Chemical
Societies Publishing

[67] Z. Zhang, B. Hong, M. Yi, X. Fan, Z. Zhang, X. Huang, Y. Lai, *Chem. Eng. J.* **2022**, *445*, 136825.

[68] P. E. Blöchl, *Phys. Rev. B* **1994**, *50*, 17953.

[69] H. J. Monkhorst, J. D. Pack, *Phys. Rev. B* **1976**, *13*, 5188.

[70] R. Dronskowski, P. E. Bloechl, *J. Phys. Chem.* **1993**, *97*, 8617.

[71] S. Maintz, V. L. Deringer, A. L. Tchougréeff, R. Dronskowski, *J. Comput. Chem.* **2013**, *34*, 2557.

[72] S. Maintz, V. L. Deringer, A. L. Tchougréeff, R. Dronskowski, *J. Comput. Chem.* **2016**, *37*, 1030.

[73] W. Xu, P. A. Russo, T. Schultz, N. Koch, N. Pinna, *ChemElectroChem* **2020**, *7*, 4016.

[74] S. P. Madhusudanan, B. Gangaja, A. G. Shyla, A. S. Nair, S. V. Nair, D. Santhanagopalan, *ACS Sustainable Chem. Eng.* **2017**, *5*, 2393.

[75] J.-H. Jeong, D. Jung, E. W. Shin, E.-S. Oh, *J. Alloys Compd.* **2014**, *604*, 226.

[76] W. Zhang, W. Zhou, J. H. Wright, Y. N. Kim, D. Liu, X. Xiao, *ACS Appl. Mater. Interfaces* **2014**, *6*, 7292.

[77] Z. Ali, S. N. Cha, J. I. Sohn, I. Shakir, C. Yan, J. M. Kim, D. J. Kang, *J. Mater. Chem.* **2012**, *22*, 17625.

[78] Y. Xing, S. Wang, B. Fang, G. Song, D. P. Wilkinson, S. Zhang, *J. Power Sources* **2018**, *385*, 10.

[79] C. Zhang, Y. Qi, S. Liu, Y. Men, F. Cui, *Mater. Chem. Phys.* **2019**, *237*, 121822.

[80] H.-G. Jung, C. S. Yoon, J. Prakash, Y.-K. Sun, *J. Phys. Chem. C* **2009**, *113*, 21258.

[81] D. P. Opra, S. V. Gnedenkov, S. L. Sinebryukhov, E. I. Voit, A. A. Sokolov, A. Y. Ustinov, V. V. Zheleznov, *Prog. Nat. Sci. Mater. Int.* **2018**, *28*, 542.

[82] M. Fehse, S. Cavaliere, P. E. Lippens, I. Savych, A. Iadecola, L. Monconduit, D. J. Jones, J. Rozière, F. Fischer, C. Tessier, L. Stievano, *J. Phys. Chem. C* **2013**, *117*, 13827.

[83] Y. Wang, T. Chen, Q. Mu, *J. Mater. Chem.* **2011**, *21*, 6006.